Chapter 5

Betatron Coupling: Measurements at RHIC with AC Dipoles

5.1 Introduction

RHIC operates very close to the difference coupling resonance $Q_x = 28.23$, $Q_y = 29.22$. This region helps maximize the available "tune space" and avoid any overlap with lattice and spin resonances. It is favorable to operate near the difference resonance to alleviate beam-beam effects and maximize the dynamic aperture. The ability to operate near the difference resonance depends on minimizing the ΔQ_{min}. Therefore, it is important to identify the coupling sources in RHIC and compensate them with available skew quadrupoles, both locally and globally. RHIC has the following relevant sources of transverse coupling:

- Skew quadrupole errors in the interaction region (IR) magnets
- Rolls in the triplet and arc quadrupoles
- Skew quadrupole families in the arc
- IR skew quadrupole correctors
- Sextupole feed-down to skew quadrupole field at the chromaticity sextupoles and at all the dipoles due to vertical closed orbit offsets.
- Experimental Solenoids

The major sources of the coupling are expected from triplet rolls where the β functions are the largest. Independently powered IR skew quadrupoles are used to compensate individual triplet rolls. This chapter aims at localizing any uncompensated coupling errors in the RHIC lattice using the techniques

described in chapter 4 and optimize the IR skew quadrupole settings. The residual coupling from the rest of the lattice is expected to be corrected using three skew quadrupole families which is discussed in section **??**.

5.2 Baseline Measurements of coupling RDT's and $|\overline{\mathbf{C}}|/\gamma^{\mathbf{2}}$

A variety of techniques to measure RDT's and the **C** matrix exist. Equivalence relations between the RDT's and **C** matrix were derived together with extensions to the existing techniques of measurement using BPM turn-by-turn data in chapter 4 and in Ref. [62]. RHIC is uniquely equipped with two AC dipoles to excite coherent betatron oscillations in transverse planes which are routinely used to measure RHIC optics [63, 64]. An analytical formalism to measure RDT's in the presence of an ac dipole was proposed in Ref. [65] and the measurements of local and global sextupole RDT's using BPM data generated from ac dipole excitation have been demonstrated at RHIC [66]. Detailed measurements of $f_{\substack{1001\\1010}}$ and $|\overline{\mathbf{C}}|/\gamma^{\mathbf{2}}$ at RHIC during the 2005 Cu-Cu run follows.

5.2.1 Injection Energy

Beam experiments were performed during the 2005 polarized proton run to measure f_{1001} and $|\overline{\mathbf{C}}|/\gamma^{\mathbf{2}}$. The goal of these experiments was to identify and measure the magnitude the local coupling sources [1]. Global coupling was initially corrected using the skew quadrupole families to minimize the tune split ($\Delta Q_{min} < 5 \times 10^{-3}$) using a skew quadrupole modulation technique [61]. Coherent betatron oscillations in both transverse planes were driven using two ac dipoles and BPM data are simultaneously recorded. The natural betatron tunes along with the ac dipole drive tunes and amplitudes are shown in Table 5.1. The data are initially processed to remove faulty BPMs according to criteria discussed in chapter 3 and Ref. [67]. Approximately 10-15% of the BPMs were found to be consistently faulty which were not used in this analysis. Fig. 5.1 shows four measurements of f_{1001} and $|\overline{\mathbf{C}}|/\gamma^{\mathbf{2}}$ as a function of longitudinal position in the yellow ring.

[1] It must be noted that beam experiment time is extremely limited and only a few configurations of skew quadrupoles were possible with the given beam time constraints.

Table 5.1: Design tunes and AC dipole drive tunes along with drive amplitude settings at injection energy

	Yellow		Blue	
Parameter	H	V	H	V
Tunes	0.731	0.723	0.735	0.721
Drive Tune	0.74	0.719	0.745	0.712
Drive Amp [mm]	0.05	0.05	0.05	0.05
Tunes	0.735	0.706	-	-
Drive Tune	0.745	0.697	-	-
Drive Amp [mm]	3.0	3.0	-	-

Although globally decoupled, the f_{1001} and $|\overline{\mathbf{C}}|/\gamma^{\mathbf{2}}$ in the yellow ring (Fig. 5.1) shows significant variations in the ring indicating uncorrected local coupling sources. f_{1001} and $|\overline{\mathbf{C}}|/\gamma^{\mathbf{2}}$ in the blue ring (Fig. 5.2) look relatively flat and also globally well decoupled. Since, the yellow ring at injection exhibits substantial features, data sets were also taken with the global skew families turned off to capture the effects of natural skew error sources without external compensation. The coupling terms with the global families are shown in Fig. 5.3 This is to be compared with Fig. 5.1. Despite the missing BPMs, both scenarios consistently exhibit positive or negative slopes in the $|f_{1001}|$ and $|\overline{\mathbf{C}}|/\gamma^{\mathbf{2}}$ behavior in the the arc regions. This is counter intuitive to the original assumption that the coupling sources are mainly confined to IR regions. Possible reasons for the slope can be attributed to

- A systematic roll of quadrupoles (or skew quadrupole component in dipole ends) in an entire arc region. This is unlikely because any roll in the quadrupoles around the ring is likely to be random and uncorrelated and will not yield a slope behavior.

- A systematic vertical orbit displacement in the arc sextupoles. This is also unlikely because the orbit recorded by the BPMs is usually centered and any small orbit displacements maybe random in nature.

An experiment with a closed three-bump orbit displacement and its effect on the coupling terms is discussed in section 5.3.2. Simulations are also underway to use the quadrupole roll and/or sextupole orbit displacement as input variables to fit the data and identify the possible sources of slopes via fitting techniques.

5.2.2 Top Energy (Store)

An experiment similar to injection was performed at top energy for the blue and yellow rings to measure f_{1001} and $|\overline{\mathbf{C}}|/\gamma^{\mathbf{2}}$. Global coupling was initially compensated similar to injection energy and the skew families were set at nominal operating values[2]. The settings for the tunes and amplitudes for top energy in the blue ring are shown in Table 5.2.

Table 5.2: Design tunes and AC dipole drive tunes along with drive amplitude settings at top energy settings

	Blue		Yellow	
Parameter	H	V	H	V
Tune	0.684	0.694	0.697	0.685
Drive Tune	0.675	0.703	0.705	0.675
Drive Amp [mm]	2	2	3	3

The data was processed to remove faulty BPMs similar to the injection data. However, the BPMs between IR4 - IR6 (3.5 - 3.85 km) in blue ring yield a $f_{1001} = 0$ which is being investigated. Fig. 5.4 shows a measurement of f_{1001} at top energy for the blue ring. A large discontinuity in f_{1001} is observed at IR12 (2 km) and smaller ones at IR8 (0.5 km) and IR4 (3 km) which indicate local skew sources.

The yellow ring exhibits large discontinuities at IR8 (0.5 km) and IR2 (2.5 km) as shown Fig. 5.5. The slope behavior is also evident at store in the yellow ring.

5.3 A Possible Correction Strategy

RHIC is equipped with skew quadrupole correctors on either side of the IR with individual power supplies located approximately with zero phase advance to the triplet quadrupoles. The main function of these individual correctors is to compensate for roll in the triplet quadrupoles. Although the corrector pair affects global coupling, they are most effective for compensating triplet magnets in that IR.

Although the slope behavior is not well understood with an additional constraint of several missing BPMs, a possible correction strategy using in-

[2]It is almost impossible to operate without global skew families at store without beam losses due to overlap of lattice resonaces

dividually powered IR skew correctors was explored. The procedure involved a systematic scan of IR skew correctors and simultaneous measurement of $4|f_{1001}|$ and $|\overline{\mathbf{C}}|/\gamma^{\mathbf{2}}$. The goal of the scan was to minimize all local jumps and also reduce the overall amplitude of the coupling terms. Any residual coupling will be further compensated with global skew families that yields the minimum f_{1001} for the minimum achievable ΔQ_{min}. Table 5.3 shows the available IR correctors with their current settings for nominal operation.

Table 5.3: Skew quadrupole maximum strengths, and nominal settings at store and injection for the yellow ring. Note that the longitudinal location specified for the IRs are approximate.

Location	**Skew Quad Name**	**Max. Strength** kl $[m^{-1}]$	I (Amp)	**Injection** kl $[m^{-1}]$	**Store** kl $[m^{-1}]$
IR-6: 0.0 km	YO-5	0.00153	50	-0.26	-0.26
	YI-6	0.00153	50	0.07	0.07
IR-8: 0.6 km	YI-7	0.00153	50	0.36	0.36
	YO-8	0.00153	50	-1.1	-1.1
IR-10: 1.3 km	Y0-9	0.00153	50	0.7	0.7
	YI-10	0.00153	50	1.0	1.0
IR-12: 1.9 km	YI-11	0.00153	50	0.3	0.3
	YO-12	0.00153	50	0.35	0.35
IR-2: 2.5 km	YO-1	0.00153	50	0.2	0.2
	YI-2	0.00153	50	0.76	0.76
IR-4: 3.2 km	YI-3	0.00153	50	0.4	0.4
	YO-4	0.00153	50	0.5	0.5

5.3.1 IR Corrector Scan: Injection

A systematic scan of a local corrector in IR-10 (YO9) was performed as an initial experiment and f_{1001} and $|\overline{\mathbf{C}}|/\gamma^{\mathbf{2}}$ were measured as shown in Fig. 5.6. Both positive and negative deviations from its nominal value increases the global coupling which is evident from the increase in f_{1001}. Since the absolute value of the coupling term is quite large, discontinuities are not clearly visible. Therefore an effective local correction would also entail a simultaneous global family correction for each local scan value which is difficult and maybe impossible given the time available for experiments. Hence the following scans

Table 5.4: Skew quadrupole maximum strengths, and nominal settings at store and injection for the blue ring. Note that the longitudinal location specified for the IRs are approximate.

Location	**Skew Quad Name**	**Max. Strength** Setting	I (Amp)	**Injection Setting**	**Store Setting**
IR-6: 0.0 km	BI-5	0.00153	50	0.0	0.0
	BO-6	0.00153	50	-0.1	-0.1
IR-8: 0.6 km	BO-7	0.00153	50	-0.9	-0.9
	BI-8	0.00168	55	1.4	1.4
IR-10: 1.3 km	BI-9	0.00168	55	0.35	0.35
	BO-10	0.00168	55	0.65	0.65
IR-12: 1.9 km	BO-11	0.00153	50	0.5	0.5
	BI-12	0.00153	50	-0.32	-0.32
IR-2: 2.5 km	BI-1	0.00168	55	-0.2	-0.2
	BO-2	0.00168	55	1.2	1.2
IR-4: 3.2 km	BO-3	0.00153	50	0.32	0.32
	BI-4	0.00153	50	0.32	0.32

were performed with global families turned off and tunes well separated. For the following scans only the $|\overline{\mathbf{C}}|/\gamma^{\mathbf{2}}$ is shown since the corresponding $4|f_{1001}|$ shows similar behavior.

IR-4 Scan

Both correctors on either side of the IR in the 4 o'clock region (YI3 and YO4) were also scanned systematically. The coupling terms and the corresponding mean values of $|\overline{\mathbf{C}}|/\gamma^{\mathbf{2}}$ and $4|f_{1001}|$ as a function of skew corrector strength is plotted in Fig. 5.7. Similar to IR-6, the red curve in Fig. 5.7 (top) appears to have the least excursion near IR-4 region which is also close to the global minimum. The nominal value seems to be close to the optimum setting, and a small decrease in both corrector values may be of further help.

IR-6 Scan

In the 6 o'clock two correctors on either side of the IR, Y05 and YI6 were scanned systematically. The coupling terms and the corresponding mean values of $|\overline{\mathbf{C}}|/\gamma^{\mathbf{2}}$ and $4|f_{1001}|$ as a function of skew corrector strength is plotted

in Fig. 5.8. Although an optimum setting is not conclusive, the red curve in Fig. 5.8 (top) appears to have the least excursion near IR-6 region. The global minimum also occurs closer to the positive side of the corrector value spectrum.

IR-8 Scan

In the 8 o'clock region a single corrector (YO-8) was scanned systematically to investigate its effect on the locally. The coupling terms and the corresponding mean values of $|\overline{\mathbf{C}}|/\gamma^{\mathbf{2}}$ and $4|f_{1001}|$ as a function of skew corrector strength is shown in Fig. 5.9. In IR-8, the nominal value of the YO-8, similar to the red curve in Fig. 5.9 (top) seems to have the least excursion near the IR-8 region and also a relatively flat distribution elsewhere. Unfortunately, this corrector is already close to its maximum strength, and further increase might have to be accomplished from the opposite side corrector (YI-7) [3].

IR-12 Scan

A scan of a single corrector (YI11) in the 12 o'clock region was performed. The coupling terms and the corresponding mean values of $|\overline{\mathbf{C}}|/\gamma^{\mathbf{2}}$ and $4|f_{1001}|$ as a function of skew corrector strength is shown in Fig. 5.10. The YI11 corrector, although located near 2 km, seems to have a significant effect in the first part of the ring (0-1.5 km). The cyan or blue curves in Fig. 5.10 (top) has a relatively flat distribution with the least excursion in the IR-10 region. The nominal value is insufficient to compensate this IR, and an increase in the correctors (YI11, YO12, or both) should improve the coupling situation in IR-12. [4].

IR-2 Scan

Similar to IR-12, a single corrector (YO1) in the 2 o'clock region was also systematically scanned. The coupling terms and the corresponding mean values of $|\overline{\mathbf{C}}|/\gamma^{\mathbf{2}}$ and $4|f_{1001}|$ as a function of skew corrector strength is shown in Fig. 5.11. The behavior near IR-2 is rather inconclusive but the nominal setting appears to a show a larger excursion. A increase in the corrector (YO1, YO2, or both) may improve the local coupling in IR-2 and will bring the machine closer to the global minimum.

[3]Note that YI-7 corrector was not scanned for IR-8

[4]Note that YO12 corrector was not scanned for IR-12

5.3.2 Vertical Orbit Bump at 2.858 km

An experiment to investigate the effect of a vertical orbit bump on the behavior of the coupling terms was performed. A closed 3-bump was inserted in the middle of an arc between the IR-2 and IR-4 region of RHIC (2.858 km). AC dipole data with increasing amplitude of the orbit bump was taken and Fig. 5.12 shows $|\overline{\mathbf{C}}|/\gamma^{\mathbf{2}}$ and its average value as a function of orbit bump amplitude.

Although small slopes exist in the baseline measurements as shown in Fig. 5.3, the slope behavior becomes prominent with the introduction of the vertical orbit bump. Additionally, the increase in the bump amplitude only seems to increase the average value of the coupling terms with changing the behavior or the magnitude of the slope around the ring. The increase in the coupling can be attributed to the coupling induced by a vertical offset in chromaticity sextupoles located in the arcs. However, the distinct slopes cannot be directly attributed to the sextupoles because of two possible reasons:

- The vertical orbit displacements in the arcs are generally random in nature
- The polarities of the chromaticity sextupoles are alternating, which would lead one to expect an oscillating behavior rather than a consistent slope.

Simulations are being performed to investigate the effect of vertical offsets in sextupoles as variables to fit to measured data. Also, the location of the slope is far from the location of the bump pointing to a more global effect than local. Therefore, vertical offsets are not likely to be a source of the slopes but merely amplify the feature. The average value of the coupling term at nominal settings in every scan (including the orbit bump) were offset from the other values in the scan. This is most likely due to hysteresis.

5.3.3 IR Corrector Scan: Store

Additional to beam time constraints, measurements at top energy (100 GeV/n) are fairly complicated due to:

- The ramping process from injection to top energy and back is approximately 1 hr. This requires that we sustain beam at top energy for the entire beam experiment. Therefore, careful placement of betatron tunes all times is necessary to avoid any overlap with resonances which may dump the beam.

- The rigidity of the beam is quite large at 100 GeV (Au ions) requiring a sufficiently large kick when using transverse dipole kickers. This leads to large emittance dilution.

- Operating an AC dipole is tricky because of resonant excitation of the beam requiring careful choice of tunes. Although this maybe the only viable option, scanning skew correctors can easily change the tunes and possibly overlap with dangerous resonances.

Therefore, compensation of local coupling sources will be optimized at injection energy and possibly extrapolated to top energy. Future measurements will determine if further optimization of the local correctors are necessary.

5.4 Global Coupling, Correction, and Optimization

The RHIC lattice has to be globally decoupled in order to operate close to the difference betatron coupling resonance. RHIC is equipped with three families of skew quadrupoles in the arcs to compensate global coupling. The coupling vectors of these families are represented in Fig. 5.13. In addition, RHIC is also equipped with two local skew correctors in each interaction region (IR). Global coupling is routinely corrected at RHIC by minimizing ΔQ_{min} using skew families either by a tune scan, a skew quadrupole modulation technique [61], or at injection using N-turn maps [48]. Two families are enough to construct a unique coupling vector and minimize the closest tune approach. The RHIC coupling correction system consists of three families with a phase of 60° between them. Therefore, there exists an infinite number of settings for three families that minimize the closest tune approach. Assuming that the setting given by the vector (f_1, f_2, f_3) minimizes the tune split, then any other setting of the form $(f_1 + \Delta, f_2 - \Delta, f_3 + \Delta)$ with arbitrary Δ is also a local minimum of the tune split. This feature can lead to situations in which the tune split is minimum (globally decoupled) but the machine is highly coupled locally. Fig. 5.14 shows an illustration by plotting the RDT, $|f_{1001}|$ around RHIC lattice (yellow ring) for different configurations of the three families, all yielding a ΔQ_{min} of about 0.001. Although different configurations all yield a minimum tune split, $|f_{1001}|$ varies significantly for each setting. The best setting should have the lowest values without large spikes. A good recipe is to minimize the average and the standard deviation at the same time. Situations as in Fig. 5.14 may have an impact on the machine optics and must be avoided.

The measurement of the coupling RDTs and **C** matrix around the ring is the only way to ensure an optimum correction of coupling.

5.5 Conclusion

Detailed measurements of RDT's and **C** matrix elements were accomplished during the RHIC Run-2005. A systematic scan of IR skew correctors was performed for each individual IR as a possible strategy to minimize local jumps in the coupling terms. A consistent slope behavior was observed and the source of the slopes is under investigation. A vertical offset experiment helps rule out the arc sextupoles as possible sources for the slopes. It is clear that the nominal settings at injection can be improved using the information from these corrector scans to reduce the excursions and overall amplitude in the yellow ring. Appropriate extrapolation and possibly more experiments can help improve the settings at top energy. A technique using RDT's or **C** matrix to optimize the global family settings was also outlined with possible experiments during Run-2006.

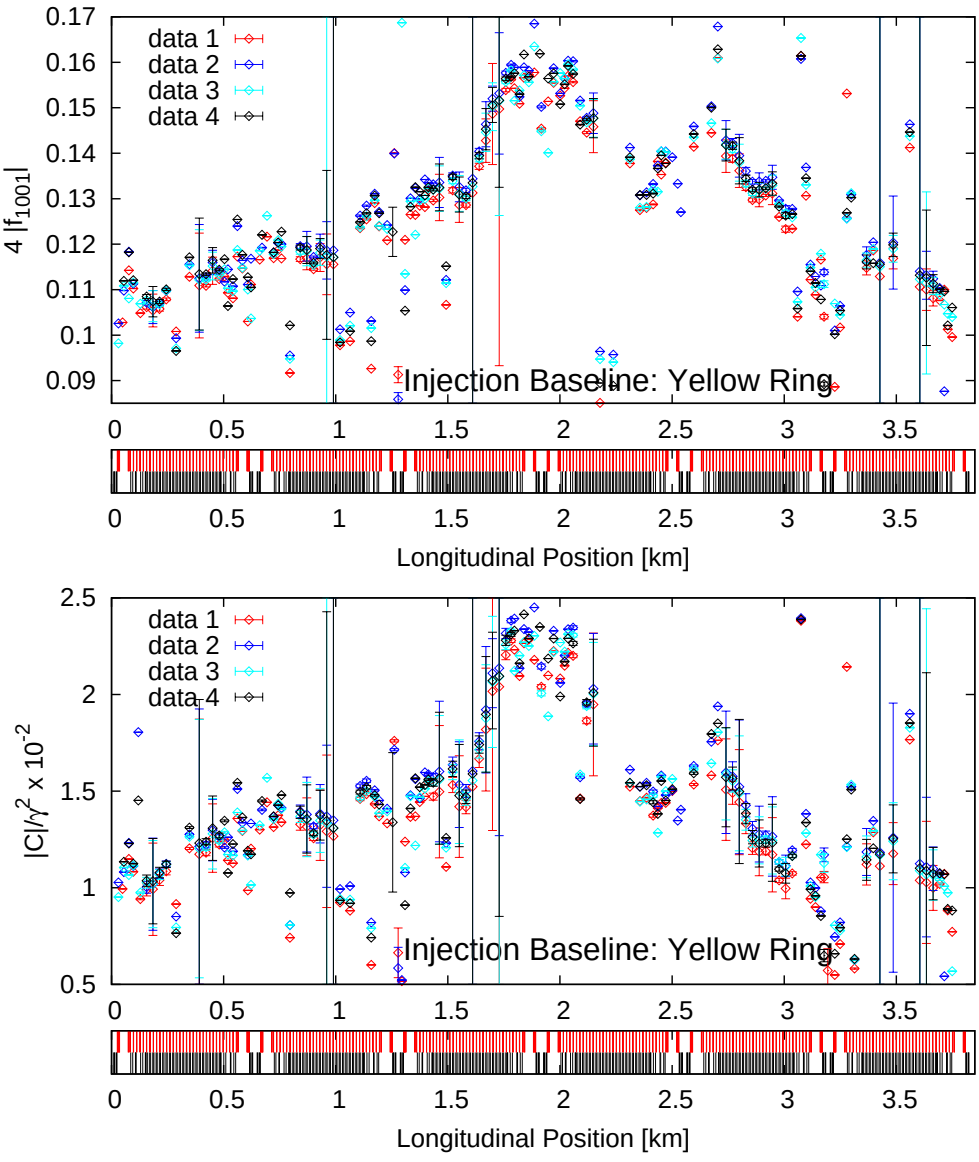

Figure 5.1: Baseline injection measurements of $4|f_{1001}|$ (top) and $|\overline{\mathbf{C}}|/\gamma^{\mathbf{2}}$ (bottom) plotted as a function of longitudinal position along the yellow ring. A representation of the lattice (dipoles in black and quadrupoles in red) is shown in the bottom graph.

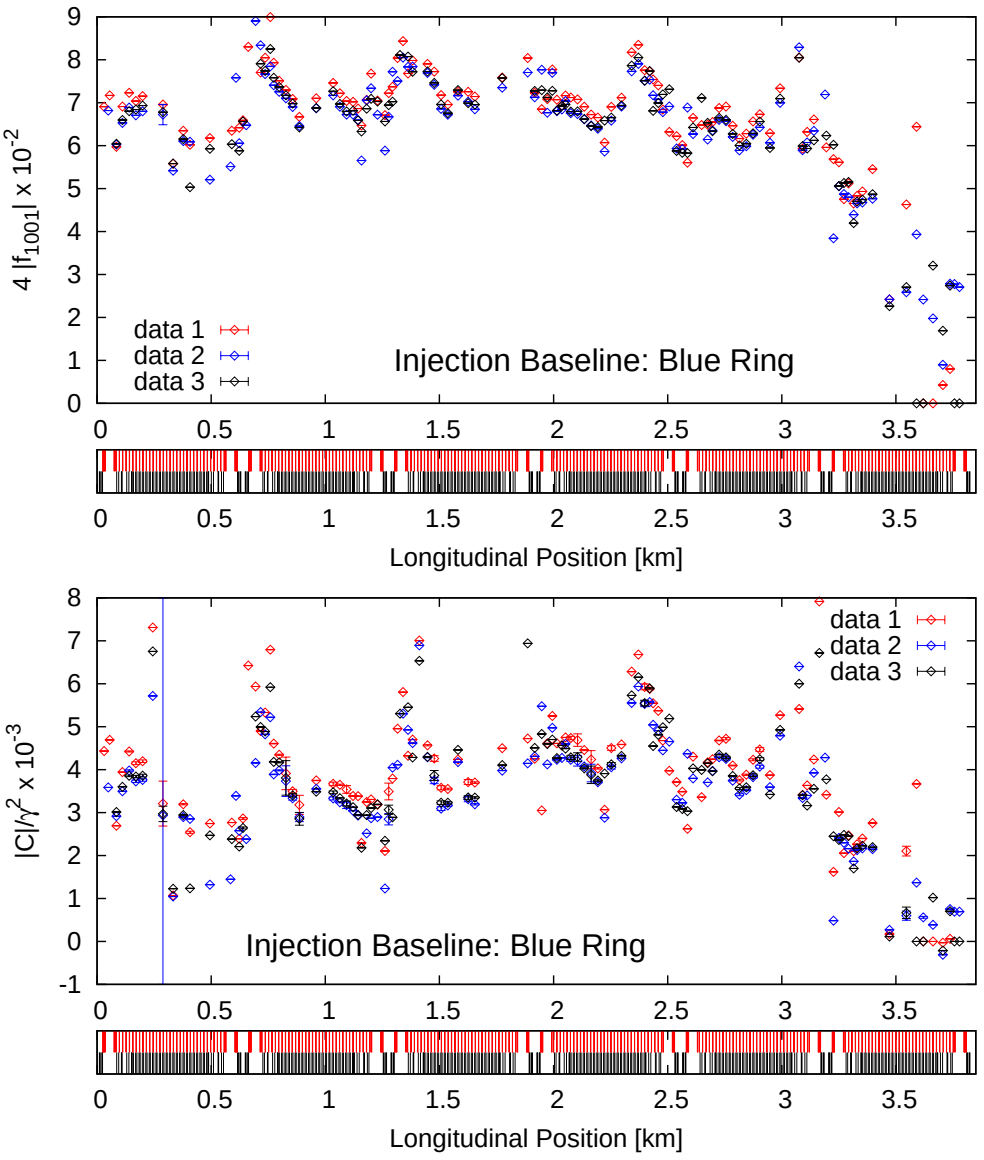

Figure 5.2: Baseline injection measurements of $4|f_{1001}|$ (top) and $|\overline{\mathbf{C}}|/\gamma^{\mathbf{2}}$ (bottom) plotted as a function of longitudinal position along the blue ring. A representation of the lattice (dipoles in black and quadrupoles in red) is shown in the bottom graph.

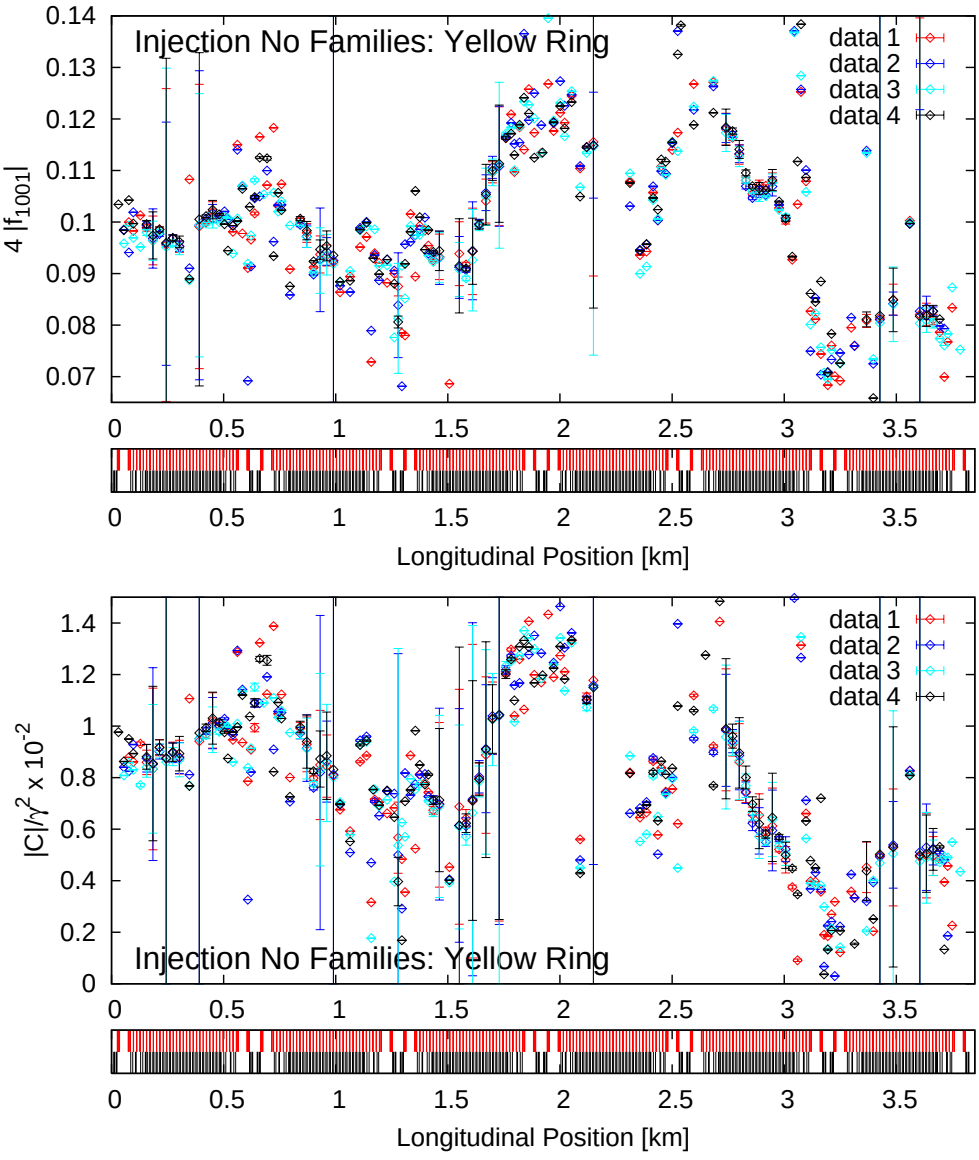

Figure 5.3: Baseline injection measurements of $4|f_{1001}|$ (top) and $|\overline{\mathbf{C}}|/\gamma^{\mathbf{2}}$ (bottom) without global skew quadrupole families plotted as a function of longitudinal position along the yellow ring. A representation of the lattice (dipoles in black and quadrupoles in red) is shown in the bottom graph.

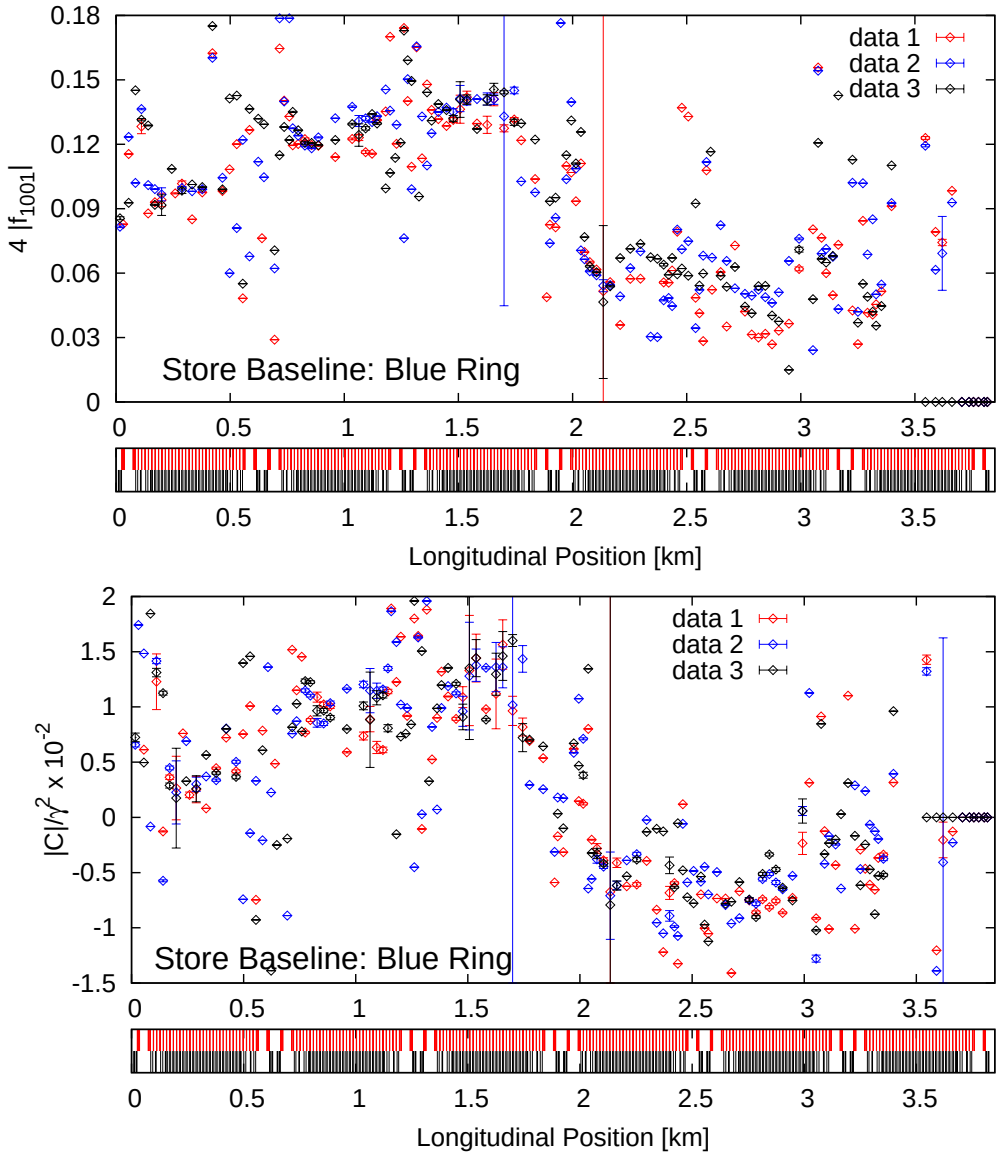

Figure 5.4: Baseline injection measurements of $4|f_{1001}|$ (top) and $|\overline{\mathbf{C}}|/\gamma^{\mathbf{2}}$ (bottom) plotted as a function of longitudinal position along the blue ring at top energy. Four data sets were taken with the same settings shown in Table 5.2. A representation of the lattice (dipoles in black and quadrupoles in red) is shown in the bottom graph.

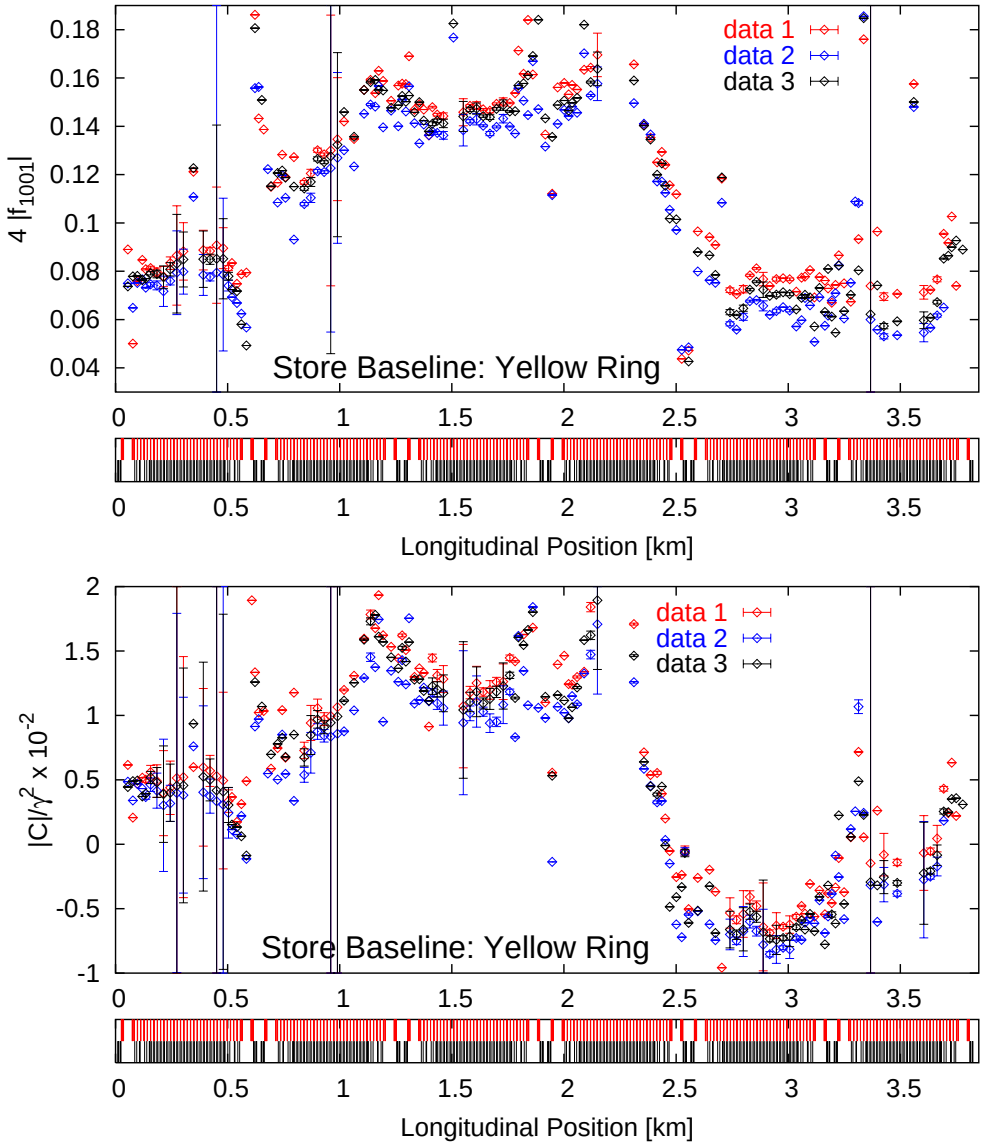

Figure 5.5: Baseline injection measurements of $4|f_{1001}|$ (top) and $|\overline{\mathbf{C}}|/\gamma^{\mathbf{2}}$ (bottom) plotted as a function of longitudinal position along the yellow ring at top energy. All four data sets were taken with the same settings shown in Table 5.2 A representation of the lattice (dipoles in black and quadrupoles in red) is shown in the bottom graph.

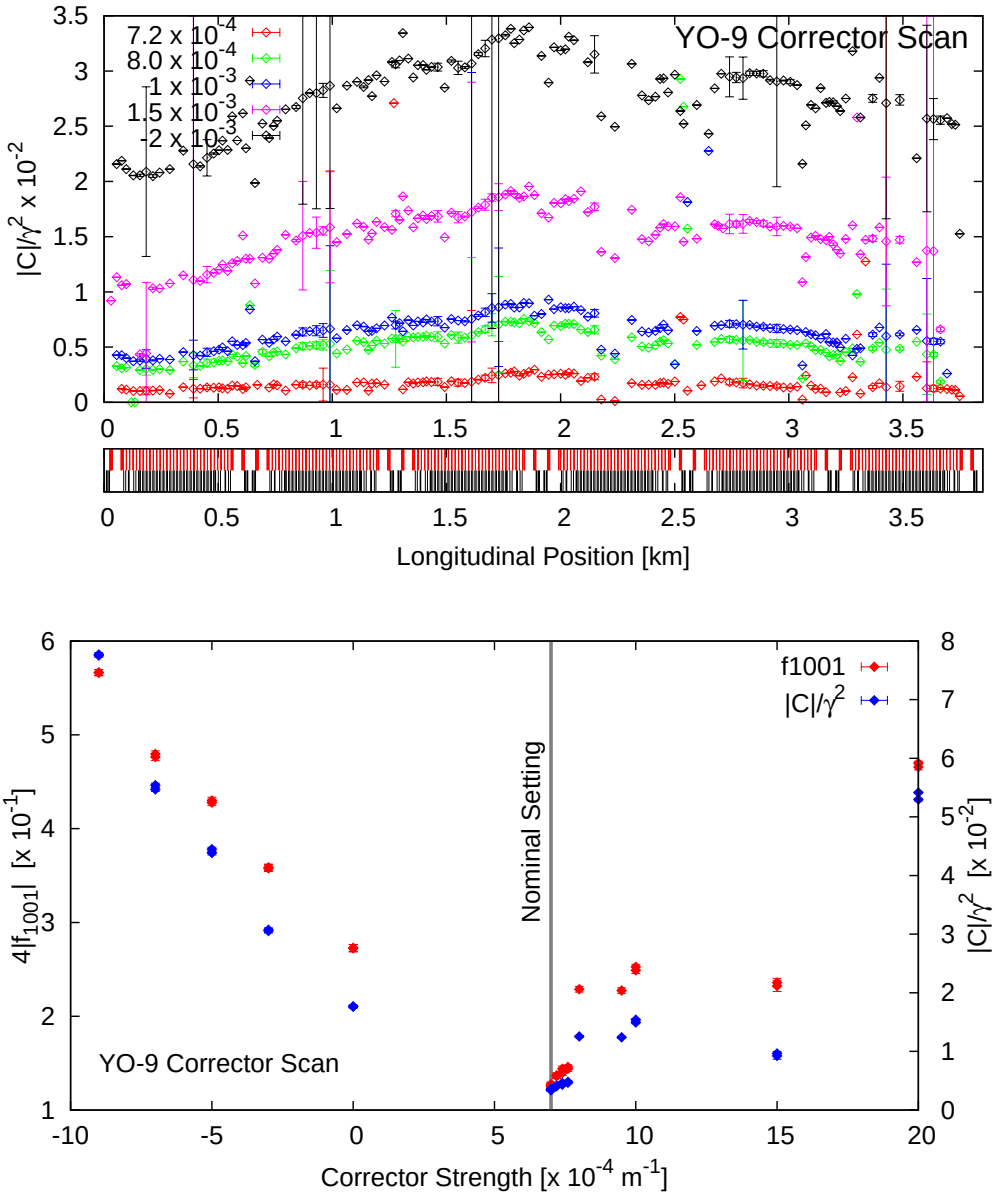

Figure 5.6: Top: $|\overline{\mathbf{C}}|/\gamma^{\mathbf{2}}$ during a positive and negative scan of YO9 corrector in IR-10 region from its nominal value as a function of longitudinal position. Bottom: The average value of $4f_{1001}$ and $|\overline{\mathbf{C}}|/\gamma^{\mathbf{2}}$ plotted as a function of the skew corrector strength. The error bars are calculated from the standard deviation of the coupling terms around the ring. Global families were compensated before the scan and drive tunes $Q_{x,y}$ and $Q^d_{x,y}$ were adjusted accordingly.

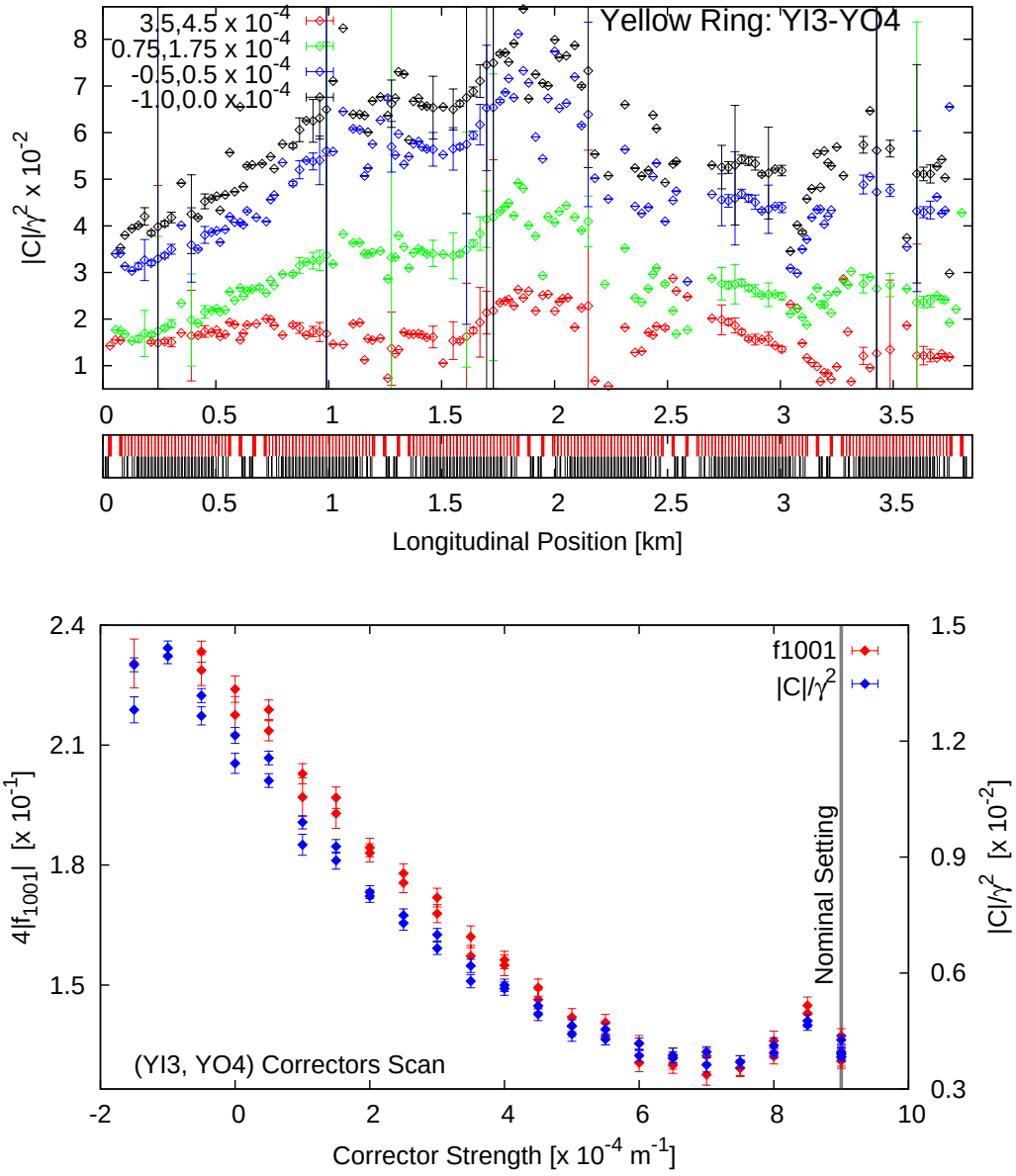

Figure 5.7: Top: $|\overline{\mathbf{C}}|/\gamma^{\mathbf{2}}$ during a scan of YI3 and YO4 correctors in IR-4 region from its nominal value as a function of longitudinal position. Bottom: The average value of $4f_{1001}$ and $|\overline{\mathbf{C}}|/\gamma^{\mathbf{2}}$ plotted as a function of the skew corrector strength. The error bars are calculated from the standard deviation of the coupling terms around the ring. Global families were turned off and t he natural and drive tunes $Q_{x,y}$ and $Q^d_{x,y}$ were adjusted accordingly.

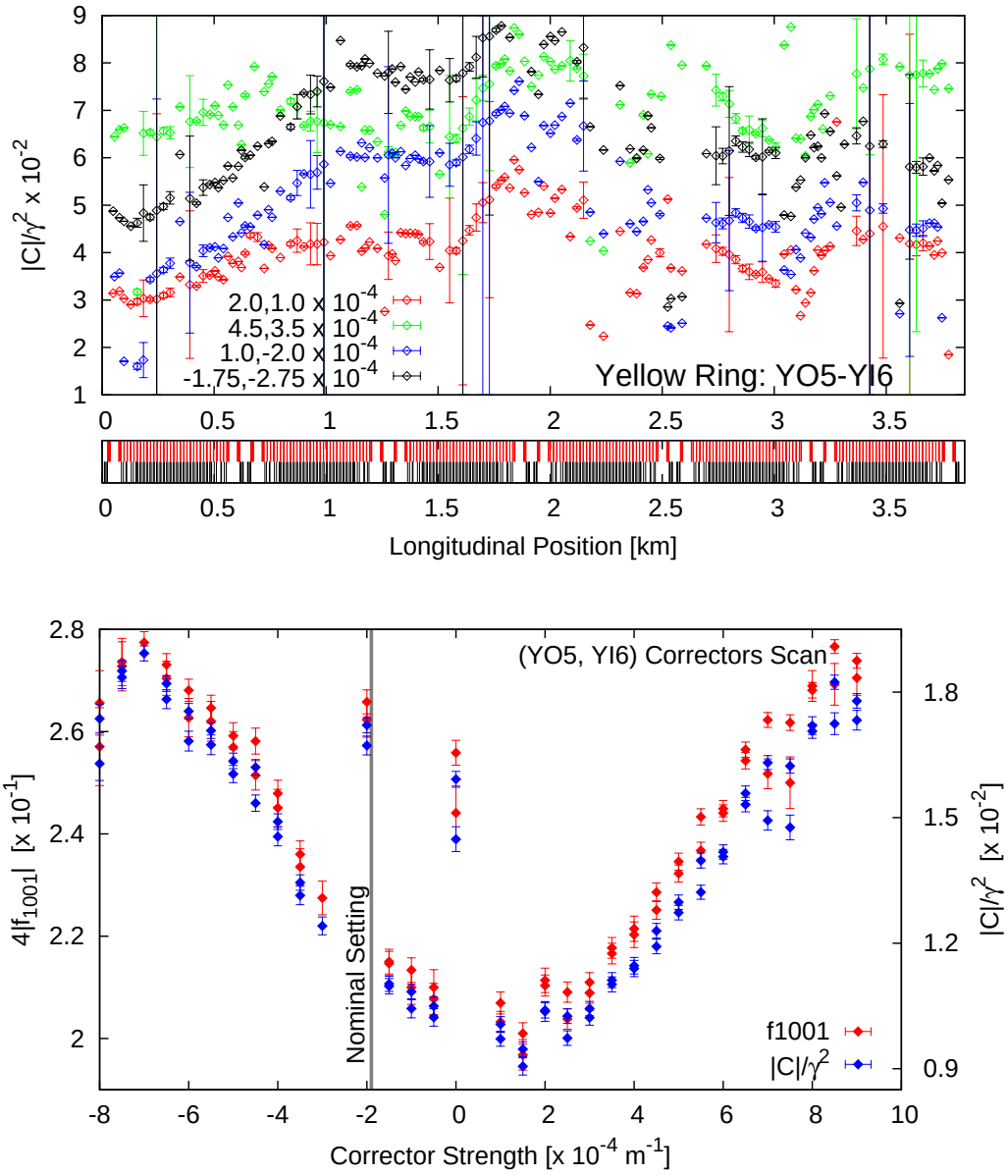

Figure 5.8: Top: $|\overline{\mathbf{C}}|/\gamma^{\mathbf{2}}$ during a positive and negative scan of YO5 and YI6 correctors in IR-6 region from its nominal value as a function of longitudinal position. Bottom: The average value of $4f_{1001}$ and $|\overline{\mathbf{C}}|/\gamma^{\mathbf{2}}$ plotted as a function of the skew corrector strength. The error bars are calculated from the standard deviation of the coupling terms around the ring. Global families were turned off and the natural and drive tunes $Q_{x,y}$ and $Q^d_{x,y}$ were adjusted accordingly.

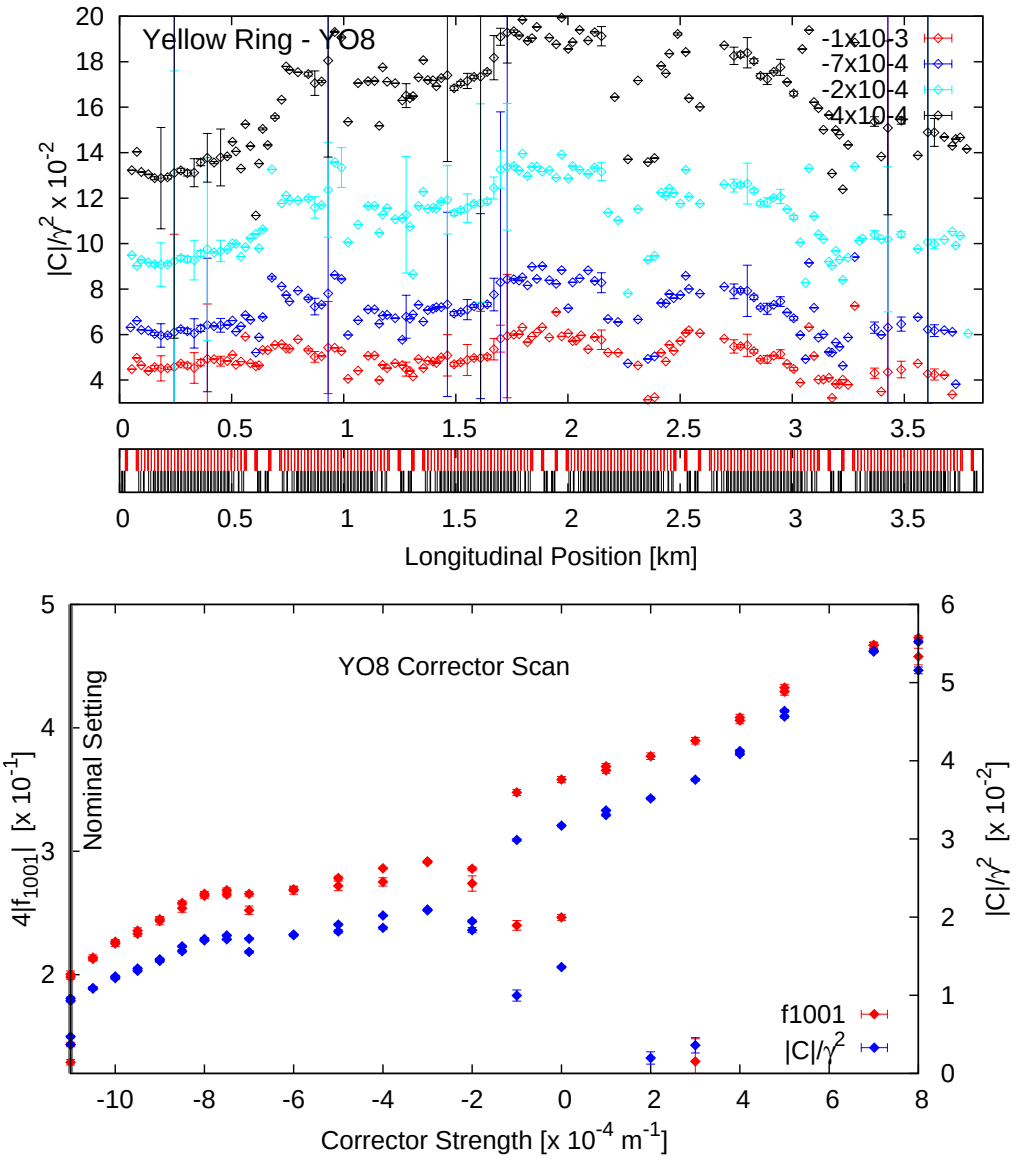

Figure 5.9: Top: $|\overline{\mathbf{C}}|/\gamma^2$ during a scan of YO-8 corrector in IR-8 region from its nominal value. Bottom: The average value of $4f_{1001}$ and $|\overline{\mathbf{C}}|/\gamma^2$ plotted as a function of the skew corrector strength. The error bars are calculated from the standard deviation of the coupling terms around the ring. Global families were turned off and the natural and drive tunes $Q_{x,y}$ and $Q^d_{x,y}$ were adjusted accordingly.

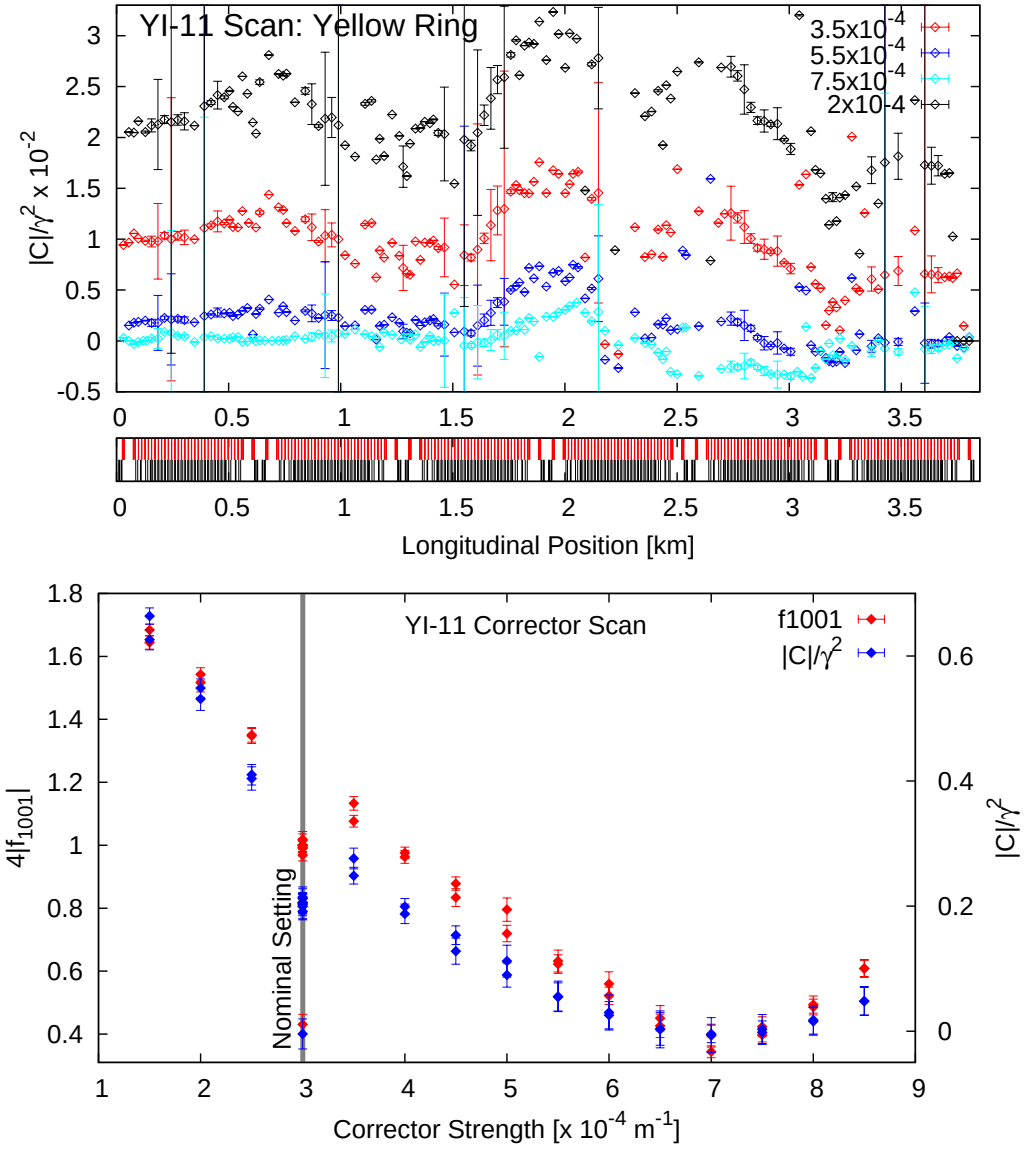

Figure 5.10: Top: $|\overline{\mathbf{C}}|/\gamma^2$ during a scan of YI11 corrector in IR-12 region from its nominal value. Bottom: The average value of $4f_{1001}$ and $|\overline{\mathbf{C}}|/\gamma^2$ plotted as a function of the skew corrector strength. The error bars are calculated from the standard deviation of the coupling terms around the ring. Global families were turned off and the natural and drive tunes $Q_{x,y}$ and $Q^d_{x,y}$ were adjusted accordingly.

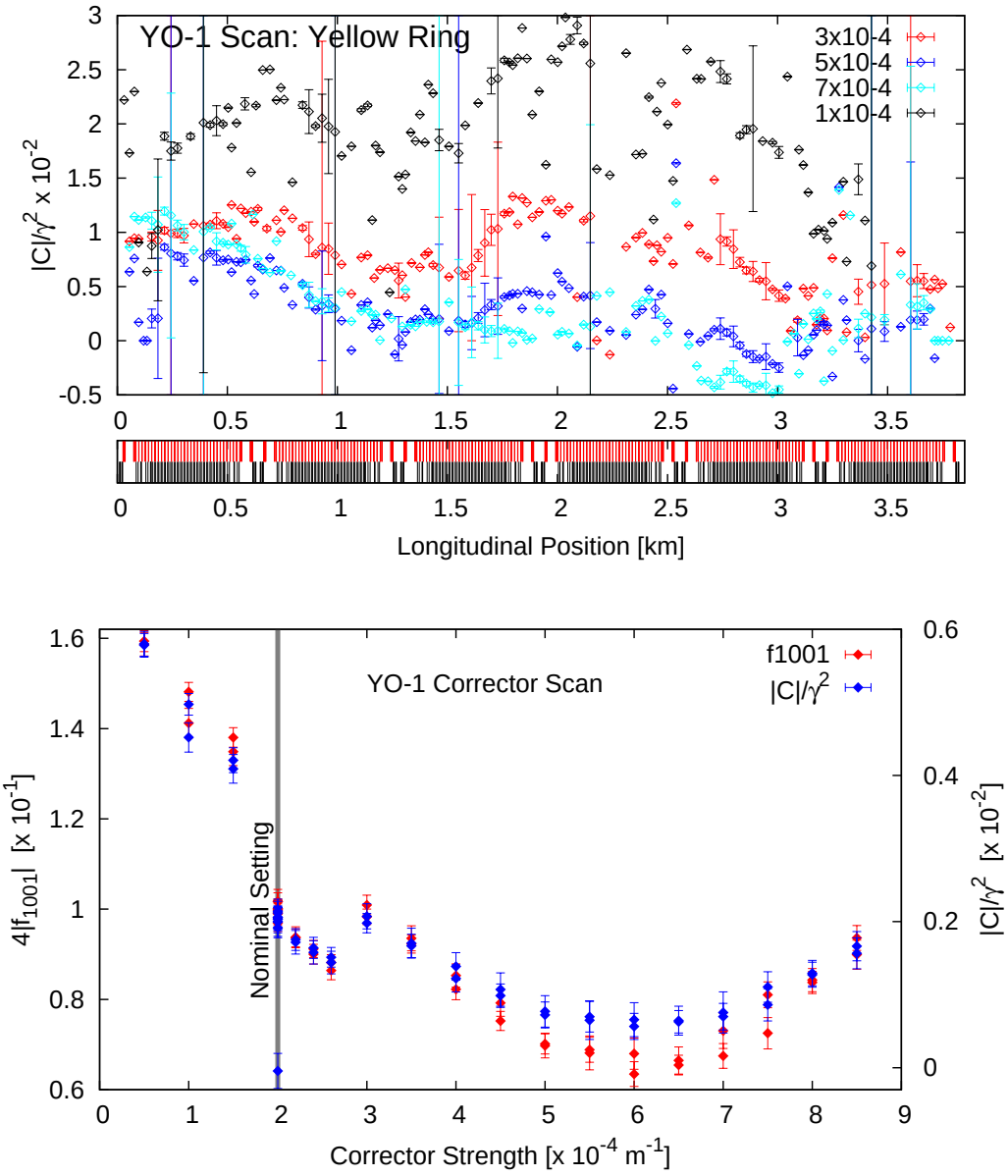

Figure 5.11: Top: $|\overline{\mathbf{C}}|/\gamma^{\mathbf{2}}$ during a scan of YO1 corrector in IR-2 region from its nominal value as a function of longitudinal position. Bottom: The average value of $4f_{1001}$ and $|\overline{\mathbf{C}}|/\gamma^{\mathbf{2}}$ plotted as a function of the skew corrector strength. The error bars are calculated from the standard deviation of the coupling terms around the ring. Global families were turned off and the natural and drive tunes $Q_{x,y}$ and $Q^d_{x,y}$ were adjusted accordingly.

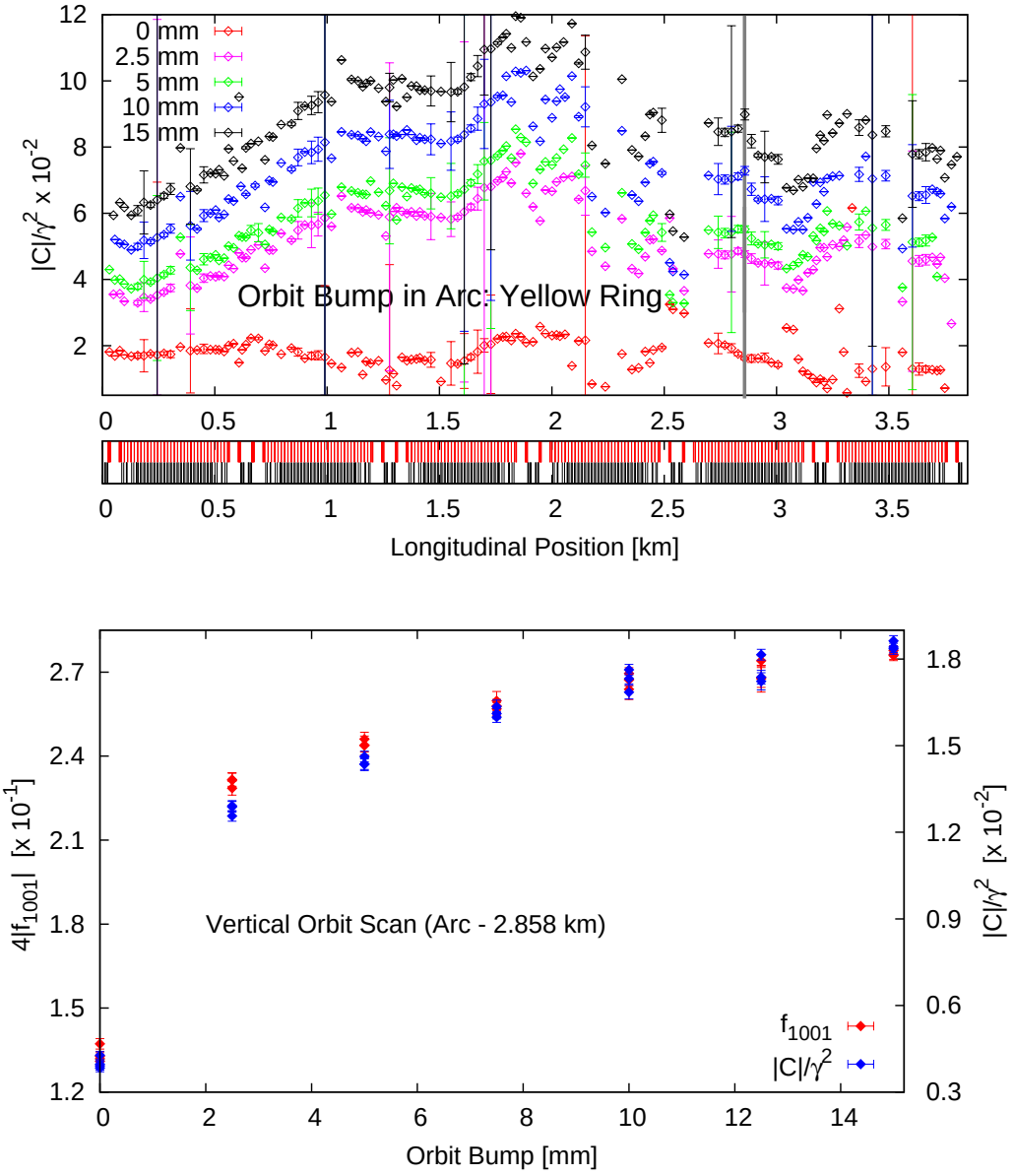

Figure 5.12: $|\overline{\mathbf{C}}|/\gamma^{\mathbf{2}}$ (top) and it's mean value (bottom) as a function the vertical orbit bump amplitude. The vertical bump was placed at 2.858 km (middle of the arc). Global families were turned off and the natural and drive tunes $Q_{x,y}$ and $Q^d_{x,y}$ were adjusted accordingly.

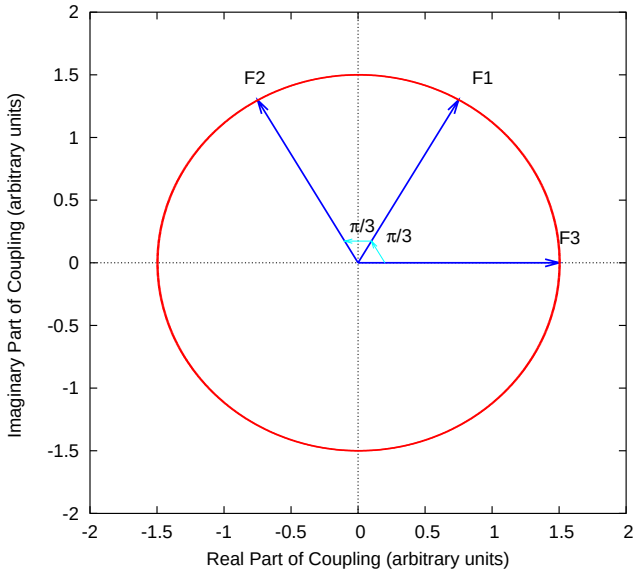

Figure 5.13: Coupling vectors of the three skew quadrupole families of RHIC (Courtesy Y. Luo).

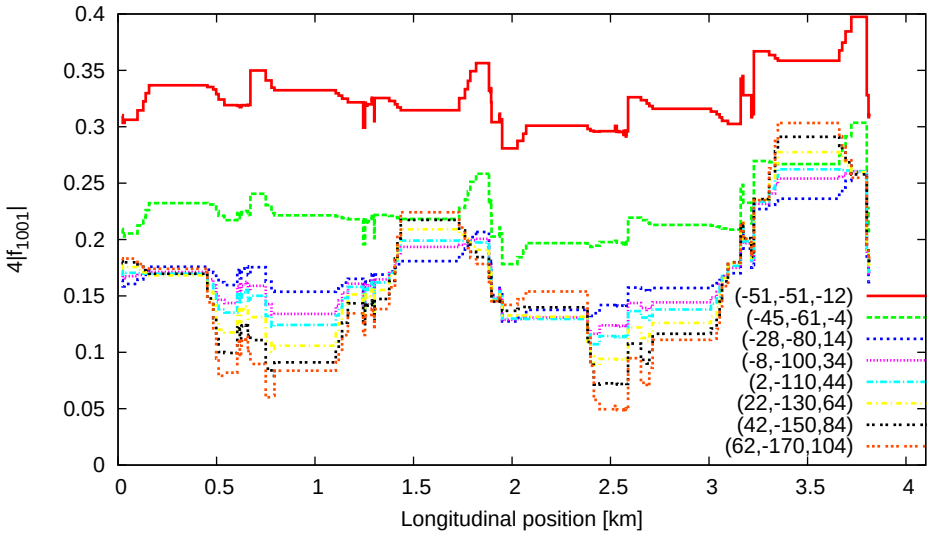

Figure 5.14: f_{1001} from model for a set of different skew families configurations. All of them have a tune split close to 0.001. The numbers in brackets represent the strength of the families in units of 10^{-5} m^{-1} (Courtesy R. Tomás).